CCS CHINESE CHEMICAL SOCIETY

ROYAL SOCIETY OF CHEMISTRY

RESEARCH ARTICLE

Check for updates

Two solvent-dependent Al₁₆ nanorings: design, synthesis and nonlinear optical limiting behavior†

San-Tai Wang,‡[a,b] Xiao Qi,‡[a,b] Ran-Qi Chen,[a] Wei-Hui Fang [iD] *[a] and Jian Zhang [iD] [a]

Cyclic compounds are of great interest to chemists for their adjustable organic shells and inorganic cores. Although the abundant bridges provide a bottom-up synthesis approach for the diversity and functionalization of ring compounds, the lack of suitable models still limits us in exploring the influence of bridge types on ring structures. Herein, we demonstrate two Al₁₆ molecular nanorings synthesized *via* 2 × 8 and 4 × 4 strategies based on the "ligand-induced aggregation and solvent regulation" strategy and discuss the influence of surface bridge flexibility on molecular ring distortion and curvature. Rigid phenol endows **AlOC-135** with unique intramolecular π⋯π interactions and higher curvature to increase the delocalization and transfer of electrons, resulting in a superior third-order nonlinear optical (NLO) response. This work provides a platform for explaining the relationship between the structure and optical properties of ring compounds at the molecular level.

Introduction

Macrocyclic molecules have attracted widespread attention due to their unique symmetry, adjustable supramolecular stacking, and central cavity for guest inclusion.[1–3] Organic–inorganic hybrid macrocycles can be directionally assembled and functionalized, enabling expansion of the applications in specific fields by altering the composition of the organic shell and inorganic metal core.[4–6] In recent decades, numerous innovative hybrid molecular ring models have emerged, such as the transition metal molecular rings Ti₃₂, Fe₃₆, Zr₇₀, Mn₈₄, Mo₁₅₄ and Mo₁₇₆.[7–12] Another big family is rare earth molecular rings such as Ln₄₂ (Yb₄₂ and Sm₄₂) bridged by acetoxy, Ce₇₀ with a sulfate linker, and the Gd₁₄₀ ring linked by 80 acetic acid molecules, 40 myo-inositol and 20 CO₃²⁻ anions.[13–15] Furthermore, heterometallic 3d–4f molecular rings are also the stars of hybrid molecular rings, such as Cr₄Dy₄, Sc₈Gd₈, and Mo₁₂₈Ce₄ with modified delta-chain structures, which are linked *via* benzoates.[16–18] These macrocyclic molecules exhibit distinct benefits in the optics, magnetism and host–guest chemistry domains.[19–23] Yang *et al.* reported a {Nd₁₈} molecular ring

exhibiting NIR luminescence sensing of antibiotics.[24] Zheng *et al.* synthesized the {Cr₈Dy₈} wheel, which is a single-molecule magnet.[25] Sun *et al.* reported the host–guest catalysis and self-assembly of Pd₂L₂ constructed from a pyridine-bonded macrocyclic ligand (L) and Pd²⁺.[26] The excellent performance of macrocyclic molecules in these fields encourages us to further develop more cyclic compounds.

Linkers are essential components of cyclic compounds and can be divided into three main groups (Scheme S1†): (a) Chelating entirely by organic linkers with coordination sites such as O_carboxyl, OH, S, and N. For example, Zhang *et al.* used *N*,*N*′-di[1-(2-hydroxyphenyl)-ethylidene]hydrazone ligand and DMF (N) as linkers to synthesize Ni₁₂.[27] Milios *et al.* synthesized Co₁₆ by salicylaldehyde bridges.[28] Besides, Baca *et al.* constructed a heterometallic ring Fe₆Dy₈ with *N*-butyl diethanolamine isobutyrate and methanol (O_hydroxyl).[29] Yamamoto *et al.* reported a series of [Pt(μ-SC₈H₁₇)₂]ₙ (*n* = 5–13) clusters with the S atom as the connection point.[30] (b) Bonding entirely with inorganic bridges. Su *et al.* synthesized [Nb₄₈V₈(OH)₃₀O₁₃₀]¹⁸⁻ using μ₂-OH⁻ as linkers.[31] Jacobson *et al.* and Wang *et al.* reported [M₈]¹⁶⁻ (M = Cr and Fe) and [Ti₈]¹⁶⁻ with μ₂-OH and μ₂-SO₄ bridges.[32,33] (c) The cooperation between organic connectors and inorganic components constitutes a ring structure. Zhao *et al.* reported on an Ln₇ ring constructed from 1,1′-cyclopropane-dicarboxylic acid and μ₃-OH inorganic linkers (Ln = Gd and Dy).[34] Zheng *et al.* synthesized Ti₃₂ constructed from acetic acid and μₙ-O (*n* = 2 or 3) linkers.[35] Christou *et al.* used triethylamine and μ₃-OH to synthesize an Fe₃₆ cluster.[12] Abundant organic/inorganic linkers provide a bottom-up synthesis approach for the diversity of

[a]*State Key Laboratory of Structural Chemistry, Fujian Institute of Research on the Structure of Matter, Chinese Academy of Sciences, Fuzhou, Fujian 350002, P.R. China. E-mail: fwh@fjirsm.ac.cn*
[b]*University of Chinese Academy of Sciences, Beijing, 100049, P.R. China*

molecular ring types and functionalization. However, exploring the influence of linker types on the ring structures is challenging.

Our group has been dedicated to the isolation of Earth-abundant element related aluminum-based molecular rings and developed the "ligand-induced aggregation and solvent regulation" strategy toward customizing ring compounds.[36,37] In previous research, we successfully expanded the Al_8 ring to the Al_{16} ring by tuning the carbon chain length of the flexible primary alcohols and developing the Al_{20} ring using a rigid phenol linker.[38,39] As a continuous work, we herein report two rings with the same nuclearity but different degrees of conjugation and study their optical properties. Considering that a ligand with a high degree of conjugation will facilitate photo-related properties, we introduced 2-naphthoic acid (2-NA) instead of the previously used benzoic acid. To investigate the effects of different auxiliary ligands (solvents) on the ring structure, we chose flexible n-propanol and rigid phenol (melting point 43 °C). With this in mind, we successfully isolated two Al_{16} molecular nanorings constructed using a 2-NA ligand but with different auxiliary bridges. The introduction of rigid phenol brings intramolecular π–π interactions, increasing the ring curvature and further influencing the intermolecular stacking, resulting in photoluminescence and nonlinear optical (NLO) changes. This study provides a platform for explaining the structure–function relationship of macrocyclic molecules at the molecular level.

Results and discussion

Synthesis discussion

2-Naphthoic acid (2-NA) plays an essential role in inducing the aggregation of Al^{3+} to form molecular rings, while phenol can be viewed as a solvent and auxiliary bridge like n-propanol. A transparent square block crystal $[Al_{16}(O^nPr)_{16}(\mu_2\text{-OH})_8(2\text{-NA})_{24}]$ (**AlOC-134**) was prepared through the one-step self-assembly method by heating $Al(O^iPr)_3$ and 2-naphthoic acid (2-NA) under the regulation of a methylaminoethanol solution and hexamethylenetetramine in a mixture of n-propanol, 1,4-dioxane and a DMF solution. When we directly added 6 mL phenol and increased the reaction temperature (100 °C to 120 °C), a light yellow oval shaped block crystal $[Al_{16}(phenol)_{20}(\mu_2\text{-OH})_8(2\text{-NA})_{20}]$ (**AlOC-135**) was successfully synthesized (Fig. 1). Although **AlOC-134** and **AlOC-135** are both 16-membered molecular rings, they exhibit different linkage modes (2 × 8 and 4 × 4 strategy).

Aluminum molecular rings supported by flexible n-propanol (2 × 8 strategy)

Single-crystal X-ray diffraction (SCXRD) showed the compound **AlOC-134** crystallizing in the monoclinic space group $C2/c$ with a total diameter of 3.1 nm, a height of about 1.9 nm, and a central hole of 0.5 nm (Fig. 2a and c). The entire molecular ring includes 16 Al^{3+} ions, 24 2-NA ligands, 16 ^{n}OPr, and eight bridged hydroxyl connections (Fig. 2a). Each aluminum ion
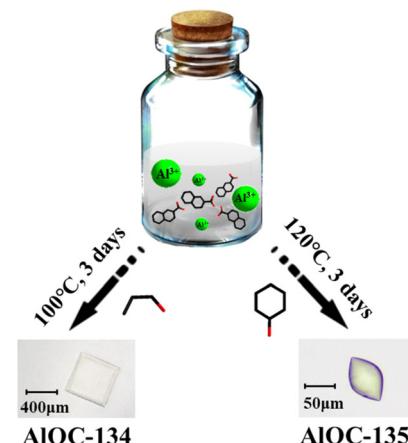

Fig. 1 "Ligand-induced aggregation and solvent regulation" synthesis of **AlOC-134** and **AlOC-135**.

adopts a six-coordinated octahedral configuration with three carboxylate oxygens (O_{COO}) from three 2-NA ligands, two hydroxyl oxygens from four ^{n}OPr ligands and one $\mu_2\text{-OH}$ (Fig. S1†), which is similar to the previously reported coordination mode of the Al_{16} ring bridged by alcohol.[38] In **AlOC-134**, the 2-NA ligand adopts the μ_2–η^1:η^1 coordination mode linking two neighbouring Al^{3+} ions to form an edge-sharing $[Al_2(^nOPr)_2(2\text{-NA})_3]$ (Al_2) dimer (Fig. 2b and S2†). Eight Al_2 dimers are connected with eight $\mu_2\text{-OH}$ to form a coronal configuration ring through the vertex sharing mode (2 × 8, Fig. S3†).

Aluminum molecular rings supported by rigid phenol (4 × 4 strategy)

When we replace the flexible n-propanol connector with rigid phenol, the Al_{16} crown-core is transformed into a twisted saddle-core (**AlOC-135**). **AlOC-135** crystallizes in the tetragonal space group $P4_2/n$ with a slightly smaller diameter (2.7 nm), a central hole of 0.4 nm and a height of about 2.3 nm (Fig. 2e and g). **AlOC-135** consists of 16 Al^{3+} ions, 20 NA^- ligands, 20 phenols and eight bridged hydroxyl groups (Fig. 2e). As shown in Fig. S1,† all Al^{3+} ions in this Al_4 tetramer have a distorted octahedral geometry: for Al_1, the coordination oxygen comes from two O_{COO} and four phenols; for Al_2, the coordination comes from two O_{COO}, three phenols, and one $\mu_2\text{-OH}$; and for Al_3, the coordination comes from three O_{COO}, one phenol, and two $\mu_2\text{-OH}$. Four 2-NA ligands adopt the same mode bridging bidentate μ_2-linking four neighbouring Al^{3+} ions to construct an edge-sharing $[Al_4(phenol)_5(2\text{-NA})_5]$ tetramer (Fig. 2f and S2†). Four independent $\mu_2\text{-OH}$ connect two adjacent Al_4 tetramers to form a saddle-shaped Al_{16} ring (4 × 4, Fig. S3†) with a bigger bending degree.

Ring curvature discussion

We tried to introduce rigid ligands with larger sizes to adjust the structural curvature, such as benzyl alcohol, 1-naphthol and 2-naphthol. Unfortunately, no related compounds were

This journal is © the Partner Organisations 2024

Inorg. Chem. Front., 2024, **11**, 462–469 | **463**
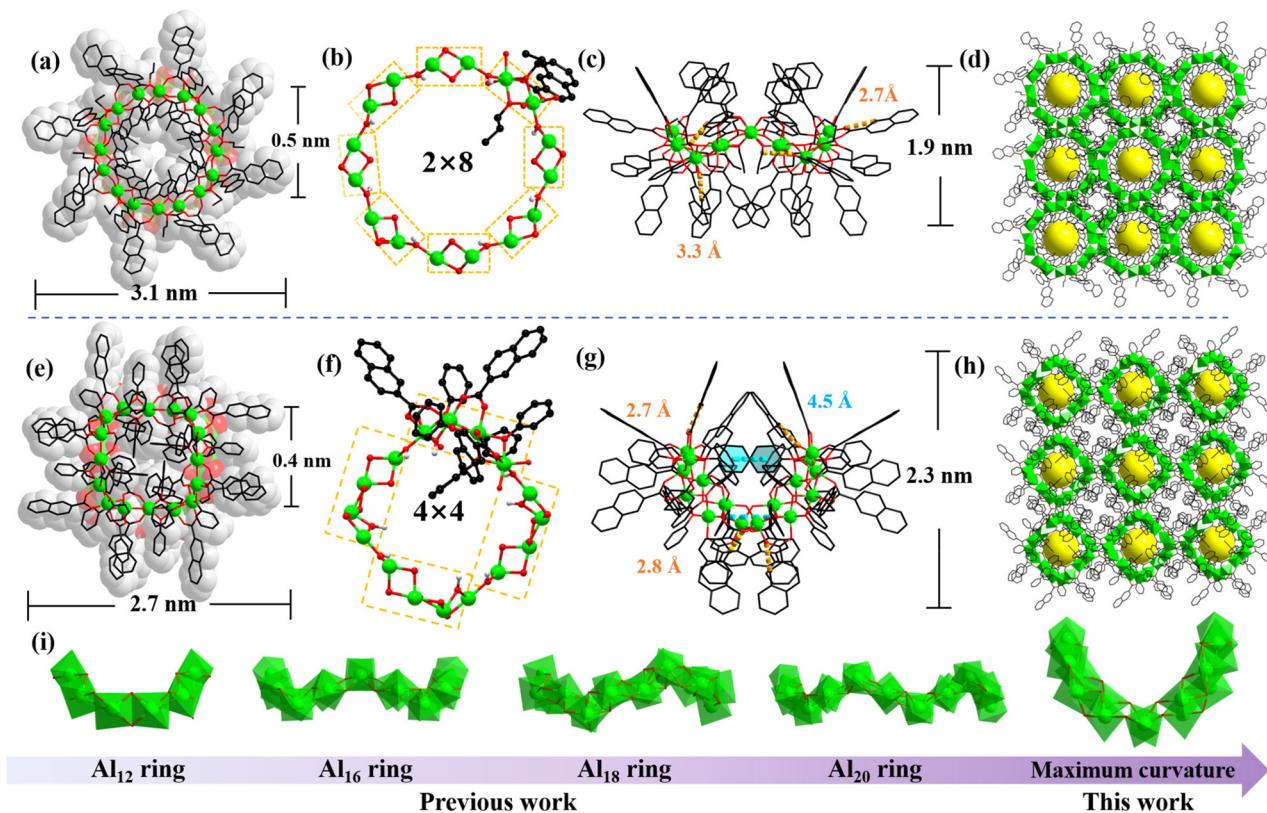
Fig. 2 Structure of **AlOC-134** and **AlOC-135**. (a) The space-filling view of **AlOC-134** (total diameter of 3.1 nm and central hole of about 0.5 nm); (b) the ball-and-stick view of the 2 × 8 ring of **AlOC-134** (Al_2 connected with μ_2-OH); (c) the side view of the corona-shaped ring of **AlOC-134** (presenting the intramolecular hydrogen bond interactions); (d) nanotube stacking diagram of **AlOC-134**; (e) the space-filling view of **AlOC-135** (total diameter of 2.7 nm and central hole of about 0.4 nm); (f) the ball-and-stick view of the 4 × 4 ring of **AlOC-135** (Al_4 connected with μ_2-OH); (g) the side view of the corona-shaped ring of **AlOC-135** (presenting the intramolecular hydrogen bond interactions and π⋯π interaction); (h) nanotube stacking diagram of **AlOC-135**; and (i) curvature changes of the aluminum molecular ring; currently **AlOC-135** has the largest curvature aluminum molecular ring. Color code: Al, green; O, red; C, black; H, grey; π⋯π interaction, blue dashed line in (g); and intramolecular hydrogen bonds, orange dashed lines in (c) and (g).

isolated, which may be attributed to their larger steric hindrance. The degree of curvature of the **AlOC-134** (crown-type) is caused by significant intramolecular hydrogen bond interactions (C–H⋯O, 2.691 Å to 3.288 Å) (Fig. 2c and Table S3†). Compared to **AlOC-134** and previous aluminum molecular rings, **AlOC-135** exhibits the most significant curvature and a rare saddle structure (Fig. 2i).[38–44] In solvent systems containing conjugated ligands, phenols with stronger polarity can easily interact with them *via* π⋯π interaction, thereby distorting the Al_{16} nucleus. This is also the reason why the amount of the linker phenol (20) is greater than that of *n*-propanol (16). Besides, the saddle-shaped conformation provides stronger supramolecular interactions within **AlOC-135**, manifested in strong hydrogen bonding interactions (C–H⋯O, 2.722–2.831 Å, Table S4†) and intramolecular π⋯π stacking interactions between phenols (4.549–4.562 Å, Fig. S4†). The two factors combine to cause the large curvature of **AlOC-135**. In both structures, all nanorings are connected to adjacent molecular rings by rich π⋯π interactions (4.129–4.869 Å, Fig. S4 and Table S5†) to form a dense array of supramolecular nanotubes. The Al–O bond lengths of two Al_{16} rings fell within the range

of 1.837–1.943 Å (Table S2†), comparable with those reported in the literature.[38,40,45] The conjugated system is instrumental in exploring the application of the two compounds in optics.

Characterization

The experimental PXRD peaks of **AlOC-134** and **AlOC-135** match well with the simulated peaks based on their space groups and cell parameters obtained using Berrar–Baldinozzi refinement. Negligible difference curves (R_{wp} and R_p values less than 5%) demonstrate the high purity of synthesized crystals (Fig. 3a and b). The energy dispersive spectroscopy (EDS) (Fig. S5 and S6†) and Fourier transform infrared spectroscopy (FT-IR) demonstrate the introduction of ligands (Fig. S7 and S8†). The vibration at 3054 cm^{-1} (**AlOC-134**) and the vibration at 3058 cm^{-1} (**AlOC-135**) are assigned to the C–H vibration of the aromatic ring. The absorption band of 3618 cm^{-1} (**AlOC-135**) is attributed to the ν(O–H) stretching on phenol; the bands at 1550 cm^{-1} (**AlOC-134**) and 1556 cm^{-1} (**AlOC-135**) can be ascribed to –CO_2^- asymmetric stretching. The bond valence sum (BVS) calculation shows that all Al ions have a +3 oxidation state (Tables S6 and S7†). The contact angle test
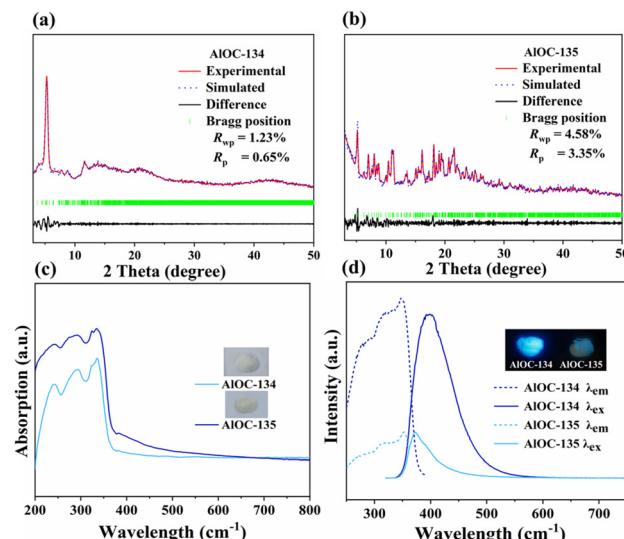
Fig. 3 (a) Simulated PXRD patterns (blue) and experimental PXRD patterns (red) of **AlOC-134**. (b) Simulated PXRD patterns (blue) and experimental PXRD patterns (red) of **AlOC-135**. (c) UV–vis diffuse reflectance spectra of **AlOC-134** and **AlOC-135** (insets are solid-state crystal samples). (d) Room-temperature photoluminescence spectra of **AlOC-134** and **AlOC-135** (inset is solid-state crystal samples under 365 nm UV light; λ_{em} is measured at an excitation wavelength of λ_{ex} = 300 nm).

reflects their excellent hydrophobicity and stability (Fig. S9†). Their thermal stability was evaluated by thermogravimetric analysis (TGA) (Fig. S10 and S11†). The solvent and air stability of the compounds are demonstrated by PXRD under different conditions, single crystal diffraction patterns and crystal pictures (Fig. 1 and S12–S14†). The excellent stability limited the dissolution of the compound in the organic solvent, which prevented further solution stability studies such as mass spectrometry.

Luminescence properties

The large π-conjugated systems and abundant supramolecular forces encouraged us to investigate their optical properties. We first explored the light absorption properties of AlOCs by measuring the UV-vis diffuse reflectance spectra. As shown in Fig. 3c, the results show that the absorption spectra of both **AlOC-134** and **AlOC-135** exhibit broad profiles ranging from 250 nm to 450 nm (Fig. S15 and S16†), which are similar to the absorption bands of 2-NA ligands (Fig. S17†). Subsequently, the fluorescence properties of the solid-state samples were measured at room temperature. As shown in Fig. 3d and S18,† the maximum emission peaks show a red shift (28 nm for **AlOC-134**, 3 nm for **AlOC-135**) at the same excitation wavelength (300 nm). Besides, **AlOC-134** has a longer lifetime and higher quantum yield (9.76 ns, 17.87%) than **AlOC-135** (2.57 ns, 7.85%) (Fig. S19 and S20†). The comparative emission spectra show that the luminescence of the nanoring can be attributed to the coordination of the 2-NA ligand with inorganic aluminum atoms.[46] The difference in

their emission intensity may be related to the quantity of the 2-NA ligands (24 in **AlOC-134** vs. 20 in **AlOC-135**) (Fig. 3d).

Third-order nonlinear optical (NLO) properties

Third-order nonlinear optics has shown potential applications in fields such as laser protection and optical switches.[47,48] The large conjugated system of Al_{16} rings encouraged us to combine crystalline materials with third-order NLO properties. The hydrophobic shell of the ring makes it less soluble and dispersible in solvents. Thus, we chose polydimethylsiloxane (PDMS, one chemically inert material with transmittance and excellent flexibility) as a solid dispersion substrate and made flexible AlOCs@PDMS films (30 mm in diameter).[49,50] All sample films had similar thicknesses and high linear transmittance (inset pictures in Fig. 4a). Open aperture (OA) Z-scan measurements were performed on solid samples under a nanosecond laser at 532 nm and a pulse energy at 80 µJ (Fig. 4a). As shown in Fig. 4b, the Z-scan curves of **AlOC-134** and **AlOC-135** display typical reverse saturation absorption (RSA) responses. The minimum normalised transmittance (T_{min}) values at the focal point were 0.84 and 0.79 for **AlOC-134** and **AlOC-135**, respectively. Such responses were reproducible and presented consistent T_{min} values, showing that the prepared samples featured excellent chemical and physical stability (Fig. S21 and S22†). According to eqn (4) and (5), the light
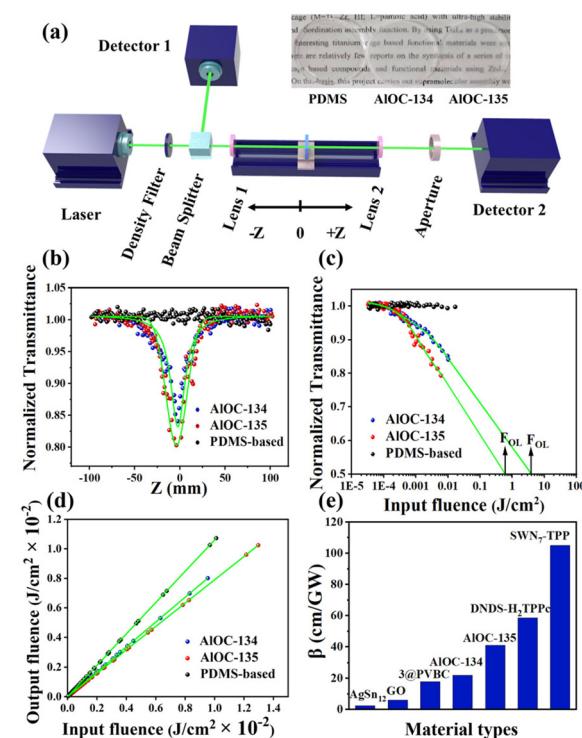

Fig. 4 (a) Schematic representation of the Z-scan setup (inset is a picture of the PDMS substrate and AlOCs@PDMS under natural light); (b) the OA Z-scan curves of input laser pulse energy 80 µJ of AlOCs@PDMS; (c) the plots of normalized transmittance versus input fluence; (d) curves of output fluence versus input fluence; and (e) the plots of comparisons of the nonlinear absorption coefficients.

This journal is © the Partner Organisations 2024

Inorg. Chem. Front., 2024, **11**, 462–469 | **465**

fluence $F_{in}(z)$ at the corresponding position z is calculated from the input laser pulse energy E_{in}. To compare the optical limiting (OL) performance, we extracted the representative OL parameter values from OL curves. Their optical limiting threshold values (F_{OL}, defined as the input fluency at 50% linear transmittance) were 3.98 J cm^{-2} (**AlOC-134**) and 0.62 J cm^{-2} (**AlOC-135**) (Fig. 4c). The curves of output fluence *versus* input fluence of such samples showed that the output fluence linearly increased at low-incident fluence. At high-incident fluence, the output fluence deviated from linearity and showed a typical OL response (Fig. 4d). The nonlinear absorption coefficient (β) (eqn (1)–(3)) of **AlOC-134** and **AlOC-135** was 22 cm GW^{-1} and 41 cm GW^{-1}, respectively. Usually, higher α and β values and lower OL values are key parameters for considering optical limiting performance. These values are not as good as those of some porphyrins and phthalocyanine materials, such as 2,9(10),16(17),23(24)-tetrakis-(4-pyridyloxy) phthalocyaninato (H$_2$TPPc) with detonation nanodiamonds in DMSO and single-walled carbon nanotube-5,10,15,20-tetraphenylporphyrin (SWN$_7$-TPP) in DMF, but superior to those of some known transition metal cluster materials, which include but are not limited to, KBr-based AgSn$_{12}$ cluster thin films, graphene oxide (GO) in DMF and [(Tp*WS$_3$Cu$_3$)$_4$(μ_4-S)$_4$(Ag)]OTf (3@PVBC) thin films (Fig. 4e and Table S9†).[51–55]

The optical limiting properties of molecular rings are closely related to the supramolecular interactions in the structure. As shown in Table S8,† **AlOC-135** has larger β and Im $\chi^{(3)}$ (eqn (6) and (7)). To find their correlation, we compared the third-order NLO effects of aluminum molecular rings with different curvatures.[39,40] However, there is insufficient evidence to prove that increasing the curvature increases the NLO effect. In this work, the introduction of phenol not only resulted in significant intramolecular $\pi\cdots\pi$ interactions but also affected intermolecular stacking, which resulted in the saddle-shaped configuration of **AlOC-135**. The synergistic interaction created by a richer conjugation interaction may directly affect the surrounding environment of the ring and its electron density, increase the delocalization and transfer of electrons, and thus produce a more obvious OL response, providing a new path for the research of enhanced light-limiting materials.

Conclusions

In summary, we demonstrated the specific application of the "ligand-induced aggregation and solvent regulation" strategy in nanoring-type regulation. Flexible *n*-propanol can generate a greater number of the components in the rings (2 × 8 strategy, **AlOC-134**). Increasing the rigidity of the solvent can reduce the crystalline symmetry and produce larger but fewer bricks (4 × 4 strategies, **AlOC-135**). Furthermore, their luminescence and third-order NLO were studied. **AlOC-134** containing more chromophores has a stronger emission intensity. Replacing *n*-propanol with phenol regulates **AlOC-135** intermolecular stacking, increases structural curvature and provides more

intramolecular $\pi\cdots\pi$ interactions. These characteristics increase the delocalization and transfer of electrons, resulting in a more pronounced NLO response. This work provides a platform for us to further understand the binding mechanism of molecular rings and their structural influence on properties at the molecular level.

Experimental

Solvothermal synthesis of (Al$_{16}$(^{n}OPr)$_{16}$(μ_2-OH)$_8$(2-NA)$_{24}$) (AlOC-134)

A mixture of Al(O^{i}Pr)$_3$ (153 mg, 0.75 mmol), 2-naphthoic acid (2-NA) (137 mg, 1.0 mmol), hexamethylenetetramine (50 mg, 0.35 mmol), methylamine solution in alcohol (50 μL), 1,4-dioxane (3 mL), *n*-propanol (5 mL), and DMF (2 mL) was sealed in a 20 mL vial and transferred to a preheated oven at 100 °C for 3 days. When cooled to room temperature, colorless transparent thin pieces of crystals were obtained (yield: 22% based on Al(O^{i}Pr)$_3$). FT-IR (cm^{-1}): 3058 (w), 2954 (w), 2360 (w), 1635 (m), 1556 (m), 1473 (m), 1421 (s) 1240 (w), 1070 (m), 965 (m), and 788 (s). The crystals were rinsed with *n*-propanol and preserved in a sealed and dry environment.

Solvothermal synthesis of (Al$_{16}$(phenol)$_{20}$(μ_2-OH)$_8$(2-NA)$_{20}$) (AlOC-135)

A mixture of Al(O^{i}Pr)$_3$ (550 mg, 2.7 mmol), 2-NA (200 mg, 1.16 mmol) and phenol (6 mL) was sealed in a 20 mL vial and transferred to a preheated oven at 120 °C for 3 days. When cooled to room temperature, colorless spheroidal crystals were obtained (yield: 13% based on Al(O^{i}Pr)$_3$). FT-IR: 3618 (w), 3054 (w), 1550 (m), 2360 (w), 1550 (m), 1481 (m), 1423 (s), 1224 (m) 1002 (w), 833 (m), and 769 (m) cm^{-1}. The crystals were rinsed with acetonitrile and preserved in a sealed and dry environment.

Caution: To avoid direct skin contact with corrosive phenol, we placed it at 80 °C for 60 minutes before use in the reaction as a solvent.

Single-crystal X-ray crystallography

Crystallographic data of **AlOC-134** and **AlOC-135** was collected on a Hybrid Pixel Array detector equipped with Ga Kα radiation (λ = 1.3405 Å) at about 298 K. The structures were determined by direct methods using Olex2 and refined with the full-matrix least-squares technique on F^2 using SHELXL. Non-hydrogen atoms were refined anisotropically.

Contact angle measurements

Contact angles were measured on powder samples using a contact angle meter with a rotatable substrate holder. 10 mg powder samples of the clusters were pressed using a glass slide to make a flat surface. A 20 μL water droplet was released slowly on the flat surface of the powder samples. Later, the droplet image was captured using a high-performance charge-coupled device (CCD) sensor. Five-point simulation analysis

466 | *Inorg. Chem. Front.*, 2024, **11**, 462–469

This journal is © the Partner Organisations 2024

was used to perform an analysis of the contact angles of all the powder samples.

Fluorescence spectroscopy measurement

Photoluminescence spectra (PL) and luminescence decay curves were performed on an Edinburgh FLS1000 fluorescence spectrometer at room temperature. All test samples were solid crystalline particles (5 mg). Emission wavelength, quantum yield and fluorescence lifetime were all measured at maximum excitation.

Preparation of AlOCs@PDMS samples

Sylgard 184 (Dow Corning) is a kit product consisting of liquid A and B components, including basic components and a curing agent. PDMS samples were fabricated using Sylgard 184 (Dow Corning) by thoroughly mixing ten parts base with one part curing agent. The fully ground AlOC samples were added to the PDMS mixture and stirred for 3 h to form AlOC dispersed PDMS suspension. Then the mixed suspension was added to a round mould, and the template was placed in a vacuum oven at 60 °C for six hours to obtain transparent and flexible AlOCs@PDMS films. The thickness of the films was measured using a digital caliper (MNT951101 manufactured by Shanghai Minette).

Third-order NLO measurement

The NLO properties of the samples were evaluated using the open-aperture (OA) Z-scan technique. The excitation light source was an Nd:YAG laser with a repetition rate of 10 Hz. The laser pulses (period, 8.5 ns; wavelength, 532 nm) were split into two beams with a mirror. The pulse energies at the front and back of the samples were monitored using energy detectors D1 and D2. All of the measurements were conducted at room temperature. The measured Z-scan curves were fitted using the following expressions:

$$T(Z, S = 1) = \frac{1}{\sqrt{\pi(Z,0)}} \int_{-\infty}^{\infty} \ln\left[1 + q_0(Z,0)e^{-r^2}\right] dr \quad (1)$$

$$q_0(Z,0) = \beta I_0 L_{eff} \quad (2)$$

$$L_{eff} = \frac{1 - e^{-al}}{\alpha} \quad (3)$$

$$F_{in}(z) = \frac{4E_{in}\sqrt{\ln 2}}{\pi^{\frac{3}{2}}\omega(z)^2} \quad (4)$$

$$\omega(z) = \frac{\omega_0}{\left[1 + \left(\frac{z}{z_0}\right)^2\right]^{-\frac{1}{2}}} \quad (5)$$

$$\text{Im}\chi^{(3)} = \frac{\lambda\varepsilon_0 c^2 n_0^2}{4\pi^2}\beta \quad (6)$$

$$\text{FOM} = \left|\frac{\text{Im}\chi^{(3)}}{\alpha}\right| \quad (7)$$

where T is the normalized transmittance, β is the nonlinear absorption coefficient, I_0 is the peak on-axis irradiance of the laser beam at the focus, L_{eff} is the effective thickness of the sample, α is the linear absorption coefficient at the laser wavelength $\left(\alpha = \ln\left(\frac{1}{T}\right)/d\right)$, z is the Z-scan displacement, ε_0 is the permittivity of vacuum (8.85×10^{-12} F m^{-1}), c is the speed of light and l denotes the thickness of the glass cell.

Data availability

The datasets supporting this article have been uploaded as part of the ESI.† CCDC reference numbers 2289659 (**AlOC-134**) and 2289660 (**AlOC-135**) contain the X-ray crystallographic data.†

Author contributions

All authors contributed extensively to the work presented in this paper. J. Zhang and W.-H. Fang conceived the research project. S.-T. Wang and X. Qi performed the synthesis, characterization, fluorescence property analysis and third-order NLO properties analysis. R.-Q. Chen assisted with the data collection and analysis. W.-H. Fang, X. Qi and S.-T. Wang wrote the manuscript and the ESI with input from the other authors.

Conflicts of interest

There are no conflicts to declare.

Acknowledgements

References

1 Y. Qin, X. Liu, P. P. Jia, L. Xu and H. B. Yang, BODIPY-based macrocycles, *Chem. Soc. Rev.*, 2020, **49**, 5678–5703.

2 M. T. Chaudhry, S. Akine and M. J. MacLachlan, Contemporary macrocycles for discrete polymetallic complexes: Precise control over structure and function, *Chem. Soc. Rev.*, 2021, **50**, 10713–10732.

3 Z. Liu, S. K. M. Nalluri and J. F. Stoddart, Surveying macrocyclic chemistry: From flexible crown ethers to rigid cyclophanes, *Chem. Soc. Rev.*, 2017, **46**, 2459–2478.

4 W. Xuan, R. Pow, D. Long and L. Cronin, Exploring the molecular growth of two gigantic half-closed polyoxometalate clusters {Mo$_{180}$} and {Mo$_{130}$Ce$_6$}, *Angew. Chem., Int. Ed.*, 2017, **56**, 9727–9731.

5 D. Lockey, C. Mathis, H. N. Miras and L. Cronin, Investigating the autocatalytically driven formation of

Keggin-based polyoxometalate clusters, *Matter*, 2022, **5**, 302–313.

6 L. Yue, K. Yang, X. Y. Lou, Y. W. Yang and R. Wang, Versatile roles of macrocycles in organic–inorganic hybrid materials for biomedical applications, *Matter*, 2020, **3**, 1557–1588.

7 S. Øien-Ødegaard, C. Bazioti, E. A. Redekop, Ø. Prytz, K. P. Lillerud and U. Olsbye, A toroidal Zr_{70} oxysulfate cluster and its diverse packing structures, *Angew. Chem., Int. Ed.*, 2020, **59**, 21397–21402.

8 A. J. Tasiopoulos, A. Vinslava, W. Wernsdorfer, K. A. Abboud and G. Christou, Giant single-molecule magnets: A {Mn_{84}} torus and its supramolecular nanotubes, *Angew. Chem., Int. Ed.*, 2004, **43**, 2117–2121.

9 C. Zhao, Y. Han, S. Dai, X. Chen, J. Yan, W. Zhang, H. Su, S. Lin, Z. Tang, B. K. Teo and N. Zheng, Microporous cyclic titanium–oxo clusters with labile surface ligands, *Angew. Chem.*, 2017, **129**, 16470–16474.

10 M. A. Moussawi, M. Haouas, S. Floquet, W. E. Shepard, P. A. Abramov, M. N. Sokolov, V. P. Fedin, S. Cordier, A. Ponchel, E. Monflier, J. Marrot and E. Cadot, Nonconventional three-component hierarchical host–guest assembly based on Mo-blue ring-shaped giant anion, γ-cyclodextrin, and Dawson-type polyoxometalate, *J. Am. Chem. Soc.*, 2017, **139**, 14376–14379.

11 H. Imai, T. Akutagawa, F. Kudo, M. Ito, K. Toyoda, S. Noro, L. Cronin and T. Nakamura, Structure, magnetism, and ionic conductivity of the gigantic {Mo_{176}} wheel assembly: $Na_{15}Fe_3Co_{16}[Mo_{176}O_{528}H_3(H_2O)_{80}]Cl_{27}\cdot450H_2O$, *J. Am. Chem. Soc.*, 2009, **131**, 13578–13579.

12 K. H. K. Lee, L. Aebersold, J. E. Peralta, K. A. Abboud and G. Christou, Synthesis, structure, and magnetic properties of an Fe_{36} dimethylarsinate cluster: The largest "ferric wheel", *Inorg. Chem.*, 2022, **61**, 17256–17267.

13 X. Y. Zheng, Y. H. Jiang, G. L. Zhuang, D. P. Liu, H. G. Liao, X. J. Kong, L. S. Long and L. S. Zheng, A gigantic molecular wheel of {Gd_{140}}: A new member of the molecular wheel family, *J. Am. Chem. Soc.*, 2017, **139**, 18178–18181.

14 D. Shi, X. Yang, H. Chen, Y. Ma, D. Schipper and R. A. Jones, Self-assembly of luminescent 42-metal lanthanide nanowheels with sensing properties towards metal ions and nitro explosives, *J. Mater. Chem. C*, 2019, **7**, 13425–13431.

15 I. Colliard, J. C. Brown, D. B. Fast, A. K. Sockwell, A. E. Hixon and M. Nyman, Snapshots of Ce_{70} toroid assembly from solids and solution, *J. Am. Chem. Soc.*, 2021, **143**, 9612–9621.

16 J. Rinck, G. Novitchi, W. V. d. Heuvel, L. Ungur, Y. Lan, W. Wernsdorfer, C. E. Anson, L. F. Chibotaru and A. K. Powell, An octanuclear [$Cr_4^{III}Dy_4^{III}$] 3d–4f single-molecule magnet, *Angew. Chem., Int. Ed.*, 2010, **49**, 7583–7587.

17 H. L. Zhang, Y. Q. Zhai, H. Nojiri, C. Schröder, H. K. Hsu, Y. T. Chan, Z. Fu and Y. Z. Zheng, {Sc_nGd_n} Heterometallic rings: Tunable ring topology for spin wave excitations, *J. Am. Chem. Soc.*, 2022, **144**, 15193–15202.

18 E. Garrido Ribó, N. L. Bell, W. Xuan, J. Luo, D. L. Long, T. Liu and L. Cronin, Synthesis, assembly, and sizing of neutral, lanthanide substituted molybdenum blue wheels {$Mo_{90}Ln_{10}$}, *J. Am. Chem. Soc.*, 2020, **142**, 17508–17514.

19 Z. Li, Y. Ye, Z. Yao, J. Guo, Q. Lin, J. Zhang, Z. Zhang, F. Wei and S. Xiang, An antiferromagnetic metalloring pyrazolate (Pz) framework with [$Cu_{12}(\mu_2\text{-OH})_{12}(Pz)_{12}$] nodes for separation of C_2H_2/CH_4 mixture, *J. Mater. Chem. A*, 2018, **6**, 19681–19688.

20 D. Gounden, N. Nombona and W. E. Van Zyl, Recent advances in phthalocyanines for chemical sensor, nonlinear optics (NLO) and energy storage applications, *Coord. Chem. Rev.*, 2020, **420**, 213359.

21 W. Xuan, R. Pow, N. Watfa, Q. Zheng, A. J. Surman, D. L. Long and L. Cronin, Stereoselective assembly of gigantic chiral molybdenum blue wheels using lanthanide ions and amino acids, *J. Am. Chem. Soc.*, 2019, **141**, 1242–1250.

22 Y. Zou, W. Lv, Z. Z. Xue, J. H. Li, X. Y. Li and G. M. Wang, Solvent-controlled synthesis of an Al_{12}-oxo molecular ring and Al_{24}-oxo truncated metallo-cube, *Inorg. Chem. Front.*, 2023, **10**, 1614–1622.

23 T. Wu, B. Han, J. X. Liu, J. Zhang, C. Xue, X. Wang and D. S. Li, A wheel-shaped gallium-sulfide molecular ring with enhanced photocatalytic activity via indium alloying, *Inorg. Chem. Front.*, 2023, **10**, 4147–4156.

24 Y. Ma, X. P. Yang, D.-L. Shi, M.-Y. Niu and D. Schipper, Construction of a 18-metal neodymium(III) nanoring with NIR luminescent sensing to antibiotics, *Inorg. Chem.*, 2020, **59**, 17608–17613.

25 L. Qin, J. Singleton, W. Chen, H. Nojiri, L. Engelhardt, R. E. P. Winpenny and Y. Zheng, Quantum Monte Carlo simulations and high-field magnetization studies of antiferromagnetic interactions in a giant hetero-spin ring, *Angew. Chem.*, 2017, **129**, 16798–16801.

26 D. Yan, L. Cai, S. Hu, Y. Zhou, L. Zhou and Q. Sun, An organo–palladium host built from a dynamic macrocyclic ligand: Adaptive self-assembly, induced-fit guest binding, and catalysis, *Angew. Chem., Int. Ed.*, 2022, **61**, e202209879.

27 Q. Liu, C. Li, B. Yao, Y. Cui, Y. Cheng, Y. Deng, Z. Chen and Y. Zhang, Self-assembly of a dodecanuclear [Ni_{12}] wheel, *Eur. J. Inorg. Chem.*, 2021, **2021**, 1305–1310.

28 P. A. Tsami, T. G. Tziotzi, A. B. Canaj, M. K. Singh, S. J. Dalgarno, E. K. Brechin and C. J. Milios, A ferromagnetically coupled pseudo-calixarene [Co_{16}] wheel that self-assembles as a tubular network of capsules, *Dalton Trans.*, 2022, **51**, 15128–15132.

29 O. Botezat, J. Van Leusen, J. Hauser, S. Decurtins, S. X. Liu, P. Kögerler and S. G. Baca, A spontaneous condensation sequence from a {Fe_6Dy_3} wheel to a {Fe_7Dy_4} globe, *Cryst. Growth Des.*, 2019, **19**, 2097–2103.

30 T. Imaoka, Y. Akanuma, N. Haruta, S. Tsuchiya, K. Ishihara, T. Okayasu, W. J. Chun, M. Takahashi and K. Yamamoto, Platinum clusters with precise numbers of atoms for preparative-scale catalysis, *Nat. Commun.*, 2017, **8**, 688.

31 Y. T. Zhang, C. Qin, X. L. Wang, P. Huang, B. Q. Song, K. Z. Shao and Z. M. Su, High-nuclear vanadoniobate

468 | *Inorg. Chem. Front.*, 2024, **11**, 462–469

This journal is © the Partner Organisations 2024

{Nb$_{48}$V$_8$} multiple-strand wheel, *Inorg. Chem.*, 2015, **54**, 11083–11087.

32 C. Liu, C. Gao, A. Said, H. Niu, D. Wang, C. H. Tung and Y. Wang, Assembly of interlocked superstructures with a titanium oxide molecular ring in water, *Inorg. Chem.*, 2021, **60**, 14520–14524.

33 M. G. Sorolla, X. Wang, T. Makarenko and A. J. Jacobson, Sulfate-bridged, octanuclear chromic and ferric wheels, *Inorg. Chem.*, 2019, **58**, 9935–9940.

34 T. Q. Song, J. Dong, A. F. Yang, X. J. Che, H. L. Gao, J. Z. Cui and B. Zhao, Wheel-like Ln$_{18}$ cluster organic frameworks for magnetic refrigeration and conversion of CO$_2$, *Inorg. Chem.*, 2018, **57**, 3144–3150.

35 C. Zhao, Y. Han, S. Dai, X. Chen, J. Yan, W. Zhang, H. Su, S. Lin, Z. Tang, B. K. Teo and N. Zheng, Ti$_{32}$ microporous cyclic titanium-oxo clusters with labile surface ligands, *Angew. Chem.*, 2017, **129**, 16470–16474.

36 D. Luo, F. Wang, C. H. Liu, S. T. Wang, Y. Y. Sun, W. H. Fang and J. Zhang, Combination of aluminum molecular rings with chemical reduction centers for iodine capture and aggregation, *Inorg. Chem. Front.*, 2022, **9**, 4506–4516.

37 J. B. Chen, S. T. Wang, S. H. Shen, Y. H. Yu, W. H. Fang and J. Zhang, In situ pyrazolylborate ligand synthesis and coordination behaviours in aluminum oxo clusters, *Inorg. Chem. Front.*, 2023, **10**, 1887–1893.

38 L. Geng, C. Liu, S. Wang, W. Fang and J. Zhang, Designable aluminum molecular rings: ring expansion and ligand functionalization, *Angew. Chem., Int. Ed.*, 2020, **59**, 16735–16740.

39 S. T. Wang, Y. J. Liu, C. C. Feng, W. H. Fang and J. Zhang, The largest aluminum molecular rings: Phenol–thermal synthesis, photoluminescence, and optical limiting, *Aggregate*, 2023, **4**, e264.

40 Y. Li, C. Zheng, S. Wang, Y. Liu, W. Fang and J. Zhang, Record aluminum molecular rings for optical limiting and nonlinear optics, *Angew. Chem., Int. Ed.*, 2022, **61**, e202116563.

41 C. Liu, W. Fang, Y. Sun, S. Yao, S. Wang, D. Lu and J. Zhang, Designable assembly of aluminum molecular rings for sequential confinement of iodine molecules, *Angew. Chem., Int. Ed.*, 2021, **60**, 21426–21433.

42 D. Luo, H. Xiao, M.-Y. Zhang, S.-D. Li, L. He, H. Lv, C.-S. Li, Q.-P. Lin, W.-H. Fang and J. Zhang, Accurate binding of porous aluminum molecular ring catalysts with the substrate, *Chem. Sci.*, 2023, **14**, 5396–5404.

43 S. Yao, W.-H. Fang, Y. Sun, S.-T. Wang and J. Zhang, Mesoporous assembly of aluminum molecular rings for iodine capture, *J. Am. Chem. Soc.*, 2021, **143**, 2325–2330.

44 Y. Zhang, Q.-H. Li, W.-H. Fang and J. Zhang, Aluminum molecular rings bearing amino-polyalcohol for iodine capture, *Inorg. Chem. Front.*, 2022, **9**, 592–598.

45 L. Geng, Q. H. Li, S. T. Wang, Y. J. Liu, W. H. Fang and J. Zhang, Aluminium nanorings: configuration deformation and structural transformation, *Chem. Commun.*, 2021, **57**, 2085–2088.

46 X.-Z. Zhang, X.-F. Wang, W.-H. Fang and J. Zhang, Synthesis, structures, and fluorescence properties of dimeric aluminum oxo clusters, *Inorg. Chem.*, 2021, **60**, 7089–7093.

47 Y. Chen, T. Bai, N. Dong, F. Fan, S. Zhang, X. Zhuang, J. Sun, B. Zhang, X. Zhang, J. Wang and W. J. Blau, Graphene and its derivatives for laser protection, *Prog. Mater. Sci.*, 2016, **84**, 118–157.

48 K. A. Green, M. P. Cifuentes, M. Samoc and M. G. Humphrey, Metal alkynyl complexes as switchable NLO systems, *Chem. Soc. Rev.*, 2011, **255**, 2530–2541.

49 W. Feng, K. Liu, J. Zang, G. Wang, R. Miao, L. Ding, T. Liu, J. Kong and Y. Fang, Flexible and transparent oligothiophene-*o*-carborane-containing hybrid films for nonlinear optical limiting based on efficient two photon absorption, *ACS Appl. Mater. Interfaces*, 2021, **13**, 28985–28995.

50 D. J. Li, Q. Li, Z. R. Wang, Z. Z. Ma, Z. G. Gu and J. Zhang, Interpenetrated metal-porphyrinic framework for enhanced nonlinear optical limiting, *J. Am. Chem. Soc.*, 2021, **143**, 17162–17169.

51 Z. K. Wang, M. H. Du, P. Braunstein and J. P. Lang, A cut-to-link strategy for cubane-based heterometallic sulfide clusters with giant third-order nonlinear optical response, *J. Am. Chem. Soc.*, 2023, **145**, 9982–9987.

52 Z. B. Liu, J. G. Tian, Z. Guo, D. M. Ren, F. Du, J. Y. Zheng and Y. S. Chen, Enhanced optical limiting effects in porphyrin-covalently functionalized single-walled carbon nanotubes, *Adv. Mater.*, 2008, **20**, 511–515.

53 J. Zhu, Y. Li, Y. Chen, J. Wang, B. Zhang, J. Zhang and W. J. Blau, Graphene oxide covalently functionalized with zinc phthalocyanine for broadband optical limiting, *Carbon*, 2011, **49**, 1900–1905.

54 R. Matshitse, S. Khene and T. Nyokong, Photophysical and nonlinear optical characteristics of pyridyl substituted phthalocyanine-Detonation nanodiamond conjugated systems in solution, *Diamond Relat. Mater.*, 2019, **94**, 218–232.

55 Y. Zhu, Z. Wang, D. Li, Y. Zhu, Q. Li, D. Li and L. Zhang, Silver-templated γ-Keggin alkyltin–oxo cluster: Electronic structure and optical limiting effect, *Angew. Chem., Int. Ed.*, 2022, **61**, e202202853.

This journal is © the Partner Organisations 2024

Inorg. Chem. Front., 2024, **11**, 462–469 | **469**